Low-energy α-nucleus optical potential studied via (α, n) cross section measurements on Te isotopes

Zs. Mátyus,[1,2] Gy. Gyürky,[1,*] P. Mohr,[1] A. Angyal,[1] Z. Halász,[1] G. G. Kiss,[1] Á. Tóth,[1,2] T. Szücs,[1] and Zs. Fülöp[1]

[1]*Institute for Nuclear Research (ATOMKI), 4001 Debrecen, Hungary*

[2]*University of Debrecen, Doctoral School of Physics, Egyetem tér 1, 4032 Debrecen, Hungary*

(Received 30 November 2023; revised 5 April 2024; accepted 3 June 2024; published 18 June 2024)

Background: In several processes of stellar nucleosynthesis, like the astrophysical γ process, nuclear reactions involving α particles play an important role. The description of these reactions necessitates the knowledge of the α-nucleus optical model potential (AOMP) which is highly ambiguous at low, astrophysical energies. This ambiguity introduces a substantial uncertainty in the stellar models for predicting elemental and isotopic abundances.

Purpose: The experimental study of the AOMP is thus necessary, and can be implemented by measuring the cross section of α-induced nuclear reactions. At low energies, (α, n) reactions are suitable for such a purpose. Therefore, in the present work, the (α, n) cross sections of four Te isotopes have been measured, mostly for the first time, and compared with theoretical predictions.

Method: The (α, n) cross sections of ^{120,122,124,130}Te have been measured in the energy range between about 10 and 17 MeV using the activation method. The detection of the γ radiation following the decay of the radioactive reaction products were used to determine the cross sections.

Results: The measured cross sections are compared with statistical model calculations obtained from the widely used TALYS nuclear reaction simulation code. Predictions using various available AOMPs are investigated.

Conclusions: It is found that the recently developed Atomki-V2 AOMP provides the best description for all studied reactions, and this potential also reproduces well the total reaction cross sections from elastic scattering experiments, when they are available in literature. We recommend therefore to use the astrophysical reaction rates based on this potential for nucleosynthesis models of heavy elements.

DOI: 10.1103/PhysRevC.109.065806

I. INTRODUCTION

Stars generate energy and synthesize chemical elements through nuclear reactions. These reactions also strongly influence the evolution and final fate of stars. The most important nuclear physics quantity is the reaction cross section which determines the astrophysical reaction rates in the stellar interior. On the one hand, reaction rates for nuclear reactions with positive Q value are the basis for the energy generation in stars. On the other hand, nuclear reaction rates define the amount and abundance distribution of heavier elements produced by the stars in the various stages of their evolution.

Ideally, the cross sections of astrophysically important reactions should be known experimentally in the energy range relevant for the given stellar process (in the so-called Gamow window [1]). The typical temperatures of stars, however, result in such low energies that direct measurement of the corresponding extremely low cross sections is not possible in most of the cases. Therefore, low energy extrapolations based on theoretical considerations are almost always necessary. Various basic nuclear physics parameters are needed for such a theoretical cross section calculation.

In the wide region of chemical elements above iron, the level density of isotopes is typically so high that statistical treatment in the cross section calculations becomes possible and also often inevitable. This can be carried out by the Hauser-Feshbach approach [2]. This method requires several input parameters such as nuclear masses, level densities, γ-ray strength functions, and models describing the interaction between nuclei [3].

In various astrophysical processes, reactions involving α particles play an important role. A prime example is the astrophysical γ process [4,5], which is thought to be the main source of those heavy, proton-rich isotopes (the p-nuclei) which cannot be produced by the neutron capture based s [6,7] and r processes [8]. The γ-process proceeds mainly through γ-induced reactions, and on the proton-rich side of the valley of nuclear stability (γ, α) reactions become important. For the theoretical description of the (γ, α) reactions in the framework of the Hauser-Feshbach statistical model, the interaction of the residual nucleus and the α particle in the exit channel is based on the α-nucleus optical model potential (AOMP). This potential must be known with high accuracy in order to describe precisely the (γ, α) reactions and hence to

*Contact author: gyurky@atomki.hu

provide reliable cross section data for γ-process nucleosynthesis models.

Historically, the AOMP was studied mainly via elastic scattering reactions, and this type of reaction is still a powerful tool for such studies [9]. In a scattering experiment, however, the cross section must deviate substantially from the Rutherford scattering cross section in order to assess the AOMP. This requires relatively high energies, typically above the astrophysically relevant energy range. One of the widely used AOMPs (the so-called McFadded-Satchler potential; MCF in the following) was developed from $E_\alpha = 24.7$ MeV scattering data [10]. When a new motivation from nuclear astrophysics arose and this potential was applied at much lower energies (around 10 MeV and below), it turned out that it is not able to give a good description of the experimental data. The need for a detailed study of low energy AOMPs was thus formulated [11].

Several new AOMP models have been created since the MCF potential (see the discussion in Sec. IV) which often result in largely different cross section predictions for (γ, α) reactions. Therefore, further experimental study of the low energy AOMP is necessary in order to find the best potential models and fine tune their parameters.

Besides elastic scattering experiments, the AOMP can also be studied by measuring the cross sections of α-induced nuclear reactions [12]. The cross section measurement of radiative capture (α, γ) reactions is preferred over the direct study of (γ, α) reactions as the effect of thermal excitation is much less severe [13,14]. Unfortunately, (α, γ) reactions usually have low cross sections in the mass and energy range of the γ process which makes the experiments challenging. An alternative approach is the measurement of (α, n) reactions which have higher cross sections above their threshold. Measured (α, n) cross sections can provide information about the AOMP, as was demonstrated recently, e.g., in [15].

In addition to the γ process discussed above, (α, n) reactions have direct relevance in the modeling of the weak r process of nucleosynthesis [16,17]. Experimental reaction rate data are also needed for a better understanding of this process [18–20].

The aim of the present work is thus to measure the (α, n) cross sections of four tellurium isotopes for which no experimental data exist in the studied energy range. This paper is organized as follows: after providing some further information about the investigated reactions in Sec. II, details of the experiments are given in Sec. III and the results are presented in Sec. III D. Section IV contains the analysis of the data from the optical model point of view, while Sec. V gives a short summary and conclusions.

II. INVESTIGATED REACTIONS

Tellurium has eight stable isotopes with mass numbers and natural abundances of 120 ($0.0921\% \pm 0.0003\%$), 122 ($2.529\% \pm 0.006\%$), 123 ($0.884\% \pm 0.002\%$), 124 ($4.715\% \pm 0.012\%$), 125 ($7.048\% \pm 0.018\%$), 126 ($18.798\% \pm 0.047\%$), 128 ($31.74\% \pm 0.08\%$) and 130 ($34.16\% \pm 0.09\%$). These abundance values are taken from the latest compilation [21] and updated by the very recent precise measurement of Te isotopic ratios [22]. (α, n) reactions on these nuclei lead to various Xe isotopes; four of them (^{123,125,127,133}Xe) are radioactive.

TABLE I. Decay parameters of the Te(α, n) reaction products. The values are taken from the most recent compilations [24–27] with the exception of the ^{125}Xe half-life, where the more precise results of a recent measurement are quoted [28].

Reaction	Half-life	E_γ (keV)	Relative intensity (%)
^{120}Te (α, n) ^{123}Xe	(2.050 ± 0.014) h	148.9	49.1 ± 0.6
		178.1	15.5 ± 0.7
		330.2	8.6 ± 0.5
^{123}Xe(β^+) ^{123}I	(13.223 ± 0.002) h	159.0	83.60 ± 0.19
^{122}Te (α, n) ^{125}Xe	(16.87 ± 0.08) h	188.4	53.8[a]
		243.4	30.0 ± 0.6
		453.8	4.67 ± 0.10
^{124}Te (α, n) ^{127}Xe	(36.346 ± 0.003) d	145.3	4.26 ± 0.15
		172.1	25.4 ± 0.9
		202.9	67.8 ± 1.2
		375.0	17.1 ± 0.6
^{130}Te (α, n) ^{133}Xe^m	(2.198 ± 0.013) d	233.2	10.12 ± 0.15
^{130}Te (α, n) ^{133}Xe^g	(5.2475 ± 0.0005) d	79.6	0.44 ± 0.18
		81.0	36.9 ± 0.3

[a]No uncertainty is given in the compilation [25].

Cross section measurement of (α, n) reactions in the mass region of the γ process using neutron detection is extremely difficult due mainly to background problems caused by high cross section, neutron-emitting nuclear reactions on target impurities. Therefore, the activation method [23] is usually preferred which is based on the detection of the decay radiation of the reaction products. This technique was used in the present work and owing to the four radioactive Xe reaction products, four reaction cross sections were studied: ^{120}Te (α, n) ^{123}Xe, ^{122}Te (α, n) ^{125}Xe, ^{124}Te (α, n) ^{127}Xe, and ^{130}Te (α, n) ^{133}Xe.

The decay parameters of the reaction products taken from the latest compilations [24–27] are summarized in Table I. The β-decay of the produced Xe isotopes is followed by the emission of characteristic γ radiation. The detection of these γ rays were used for the cross section determination. The table contains only the most intense γ transitions which were used for the analysis. Besides its ground state, ^{133}Xe has a long-lived isomeric state which has decay signature different from the ground state. Therefore, in the case of the ^{130}Te (α, n) ^{133}Xe reaction, the cross sections leading both to the ground and isomeric states of ^{133}Xe could be measured.

III. EXPERIMENTAL PROCEDURE

A. Target preparation and characterization

In order to measure the (α, n) cross sections of all studied isotopes at a given energy in a single irradiation, natural isotopic composition targets were used. The targets were prepared by vacuum evaporation. High chemical purity (>99.999%) metallic Te was evaporated onto 10 μm thick Al foil backings. The foils were fixed in annular target holders

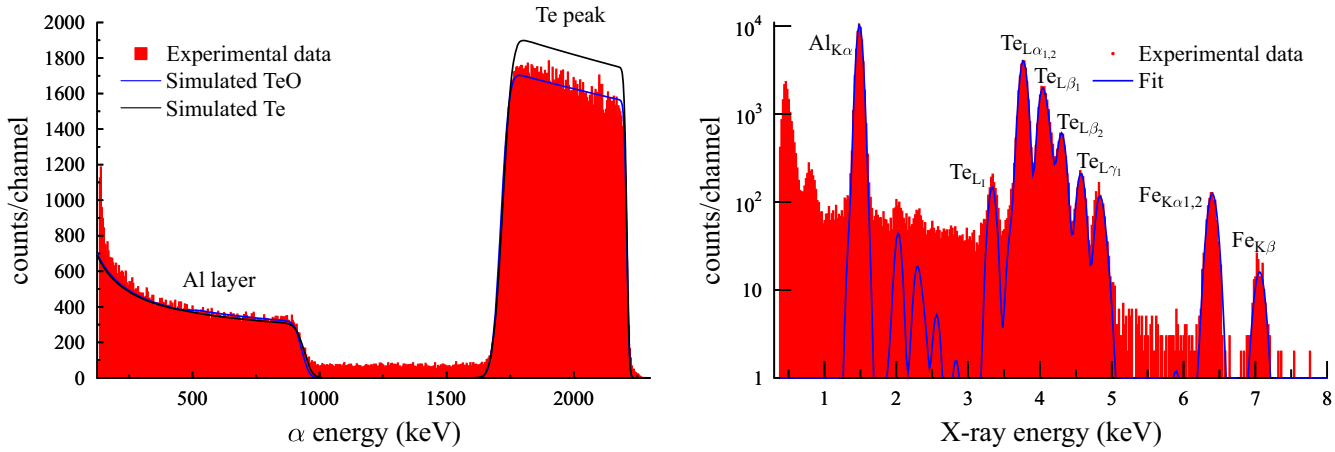

FIG. 1. Left: A measured and fitted RBS spectrum. Besides the best fit labeled as TeO, a fit supposing a pure Te layer is also shown (labeled as Te) indicating the need for including oxygen in the layer composition. Right: PIXE spectrum indicating the peaks corresponding to Te, Al, and Fe. The last one is the highest concentration impurity in the Al foil.

with 16 mm in inner diameter. The weight measurement of the Al foils with 1 μg precision before and after the evaporation provided the first information about the target thicknesses, which were typically around 600 $\mu g/cm^2$. Besides several test evaporations, eight targets were prepared and characterized as described below.

Thin layers of Te may oxidize in the residual gas of the vacuum evaporator or after the target preparation. The weight measurement of the targets, therefore, does not provide the Te target thickness (i.e., the surface number density of the Te atoms) as the Te:O stoichiometric ratio is not known *a priori*. The Te target thicknesses were thus measured with two independent ion beam analysis methods: Rutherford backscattering spectrometry (RBS) and particle-induced x-ray emission (PIXE).

The RBS measurement was carried out at the Tandetron accelerator of Atomki [29]. The targets were bombarded by a 2.5 MeV α beam with a few hundred nA intensity. The backscattered α particles were detected with an ion implanted Si detector placed at 165° with respect to the beam direction. The acquired spectra were analyzed with the SIMNRA code [30] to obtain the Te target thickness and in addition the Te:O ratio. The beam size used for the RBS measurement was similar to the one of the cross section measurement. The left panel of Fig. 1 shows a typical RBS spectrum with the best fit and with a calculated spectrum supposing a pure, oxygen-free Te layer. It can clearly be seen that, without supposing oxygen in the layer, the measured spectra cannot be reproduced. The obtained Te:O atomic ratios were typically 0.7:0.3 and Te surface densities were in the range of $(2.0–2.5) \times 10^{18}$ atoms/cm^2.

The PIXE measurements were also carried out at the Tandetron accelerator using its microbeam setup. The targets were bombarded by 3.2 MeV protons and the induced x rays were detected with an SDD detector with AP3.3 ultrathin polymer window (SGX Sesortech). A permanent magnet protected the detector from the scattered protons. The beam dose was measured with a beam chopper [31]. PIXE spectra were recorded with an SGX DX200 digital DPP and evaluated with the GUPIXWIN program code [32] in order to obtain the Te target thickness. Exploiting the capabilities of the microbeam setup, spectra were taken on three different positions on each target with a few mm apart, scanning the beam on a 1 mm × 1 mm area. Information on the target homogeneity could be obtained this way. Thicknesses measured at different positions on a given target were always in agreement within the uncertainty. Figure 1 shows a typical PIXE spectrum where the relevant peaks are indicated (right panel).

The Te thicknesses from the RBS and PIXE measurements were always in agreement, the largest deviation was 4%, well within the 5% uncertainty characteristic for both methods. The average of the two results was thus adopted as the final target thickness used for the cross section determination.

B. Irradiations

For the (α, n) cross section measurements the targets were irradiated by α beams provided by the cyclotron accelerator of Atomki [33]. The target chamber was the same as used in our recent experiments, see Fig. 3 in Ref. [34]. The typical He^{++} beam intensity was about 1 μA which was measured by a charge integrator. The fluctuations in the beam intensity were taken into account by recording the collected charge in the chamber as a function of time with 1 min time resolution.

The length of the irradiations varied between 3 and 41 hours. Longer irradiations were used at the lowest energies where the cross sections are the smallest. The studied α energy range between 10 and 17 MeV was covered with 1 MeV steps, eight irradiations were thus carried out. The lowest measurable energy was determined by the dropping cross section, below this energy the cross sections could not be determined with reasonable precision. Energies higher than 17 MeV were not studied, on the one hand because of the decreasing astrophysical relevance and on the other hand because of the opening of other reaction channels, as will be discussed in Sec. III D.

Due to technical reasons, the cyclotron accelerator could not provide a 10 MeV α beam. Therefore, the lowest energy

point was measured using an energy degrader foil. An Al foil of 10.14 μm thickness was placed in front of the Te target. The precise thickness of the degrader foil was determined by α-energy loss measurement. The spectrum of α particles from a mixed ^{239}Pu-^{241}Am-^{244}Cm calibration source after passing through the foil was measured in an alpha spectrometer. Based on the stopping power of Al obtained from the SRIM code [35], the foil thickness was determined with 4% accuracy. This results was used to obtain the interaction energy at the Te target.

C. Detection of the decay radiation

After the irradiations, the targets containing the created reaction products were removed from the irradiation chamber and transported to a γ detector setup for ofline decay counting. As it can be seen in Table I, the decay of the reaction products is mainly followed by low-energy γ radiation. Therefore, a planar detector consisting of a Ge crystal with 60.7 mm diameter and 26.4 mm thickness and a thin carbon epoxy window was used which has high efficiency for low energy γ rays, good energy resolution, and—owing to the small crystal size—relatively low background caused by higher energy γ radiation. For the first two measurements (at 12 and 17 MeV α energies), however, the planar detector was not available. Therefore, for these runs a 100% relative efficiency coaxial high-purity germanium (HPGe) detector was used. Both detectors were put in complete 4π lead shielding against laboratory background.

The absolute detection efficiency of the detectors was measured with calibrated ^{133}Ba, ^{137}Cs, and ^{152}Eu standard sources. The efficiency measurements were carried out at two geometries in the case of both detectors: the distance between the source and the detector surface was 10 and 17 cm at the planar detector and 10 and 27 cm at the coaxial detector. At these relatively far distances the true coincidence summing effect is negligible (below 1%), thus the multiline calibration sources can be used to obtain a smooth energy-efficiency function. As an example, the measured and fitted efficiency of the planar detector can be seen in Fig. 2.

At the lowest measured energies, however, the small cross sections necessitated the γ counting in close geometry, placing the targets at 1 cm from the detector surface. At such a distance the direct measurement of the efficiency is hampered by the true coincidence summing effect. Such a direct measurement was thus not made. The two-distance method [23] was used instead to indirectly determine the detection efficiency for the relevant γ energies. The activity of some Te targets irradiated at higher α energies was measured at the 1 cm distance as well as at larger distances where the direct efficiency measurements were implemented. Distance conversion factors were then calculated for all relevant γ energies. These conversion factors already include the effect of summing at close distances which is thus naturally accounted for.

As it is evident from Fig. 2, the lowest energy measured efficiency points (at 79.6 and 81.0 keV from ^{133}Ba) are well below the fitted curve. These energies are important for the ^{130}Te (α, n) ^{133}Xe^{g} reaction. However, since the decay of

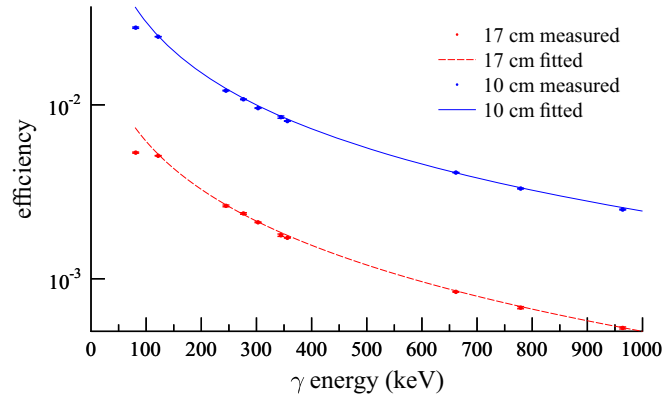

FIG. 2. Full-energy peak efficiency of the planar detector at two source-to-detector distances. The efficiencies measured with calibration sources as well as their fitted curves are shown. The fitted efficiencies were used at the relevant γ energies with the exception of the 79.6 and 81 keV lines from ^{133}Xe^{m}. At these energies the fitted curves clearly deviate from the measured point. For these transitions, the efficiency measured directly with the ^{133}Ba source was used, which has its γ lines at these energies.

^{133}Xe^{g} involves the emission of the same γ radiation as the ^{133}Ba calibration source, in the case of the 79.6 and 81.0 keV lines the directly determined efficiency value was used instead of the fitted curve.

Figure 3 shows a typical γ spectrum measured with the planar detector at 10 cm distance on the target irradiated with a 16 MeV α beam. The peaks corresponding to the transitions listed in Table I are indicated.

D. Results

Tables II–V show the obtained cross section results for the four studied reactions, respectively. Owing to the very small natural abundance of ^{120}Te, the yield of ^{120}Te (α, n) ^{123}Xe was too small at the lowest measured energy of $E_\alpha = 10$ MeV. The cross section of all other studied reaction channels was measured in the 10–17 MeV energy range.

The first column of the Tables shows the primary beam energies as provided by the cyclotron. These energy values have an uncertainty of 0.3% from the accelerator energy calibration. The only exception is the lowest energy measurement where a degrader foil was applied, as discussed in Sec. III B.

TABLE II. Experimental cross section and S-factor results of the ^{120}Te (α, n) ^{123}Xe reaction. See text for details.

E_α (MeV)	$E_{\text{c.m.}}^{\text{eff}}$ (MeV)	Cross section (mb)	S factor (10^{25} keV b)
11.0	10.586 ± 0.072	0.336 ± 0.134	385 ± 154
12.0	11.557 ± 0.070	1.80 ± 0.23	156 ± 20
13.0	12.525 ± 0.071	13.1 ± 1.0	117 ± 9
14.0	13.497 ± 0.069	49.9 ± 3.9	58.9 ± 4.7
15.0	14.468 ± 0.068	142 ± 12	27.3 ± 2.3
16.0	15.438 ± 0.068	260 ± 21	9.8 ± 0.8
17.0	16.410 ± 0.066	345 ± 27	2.93 ± 0.23

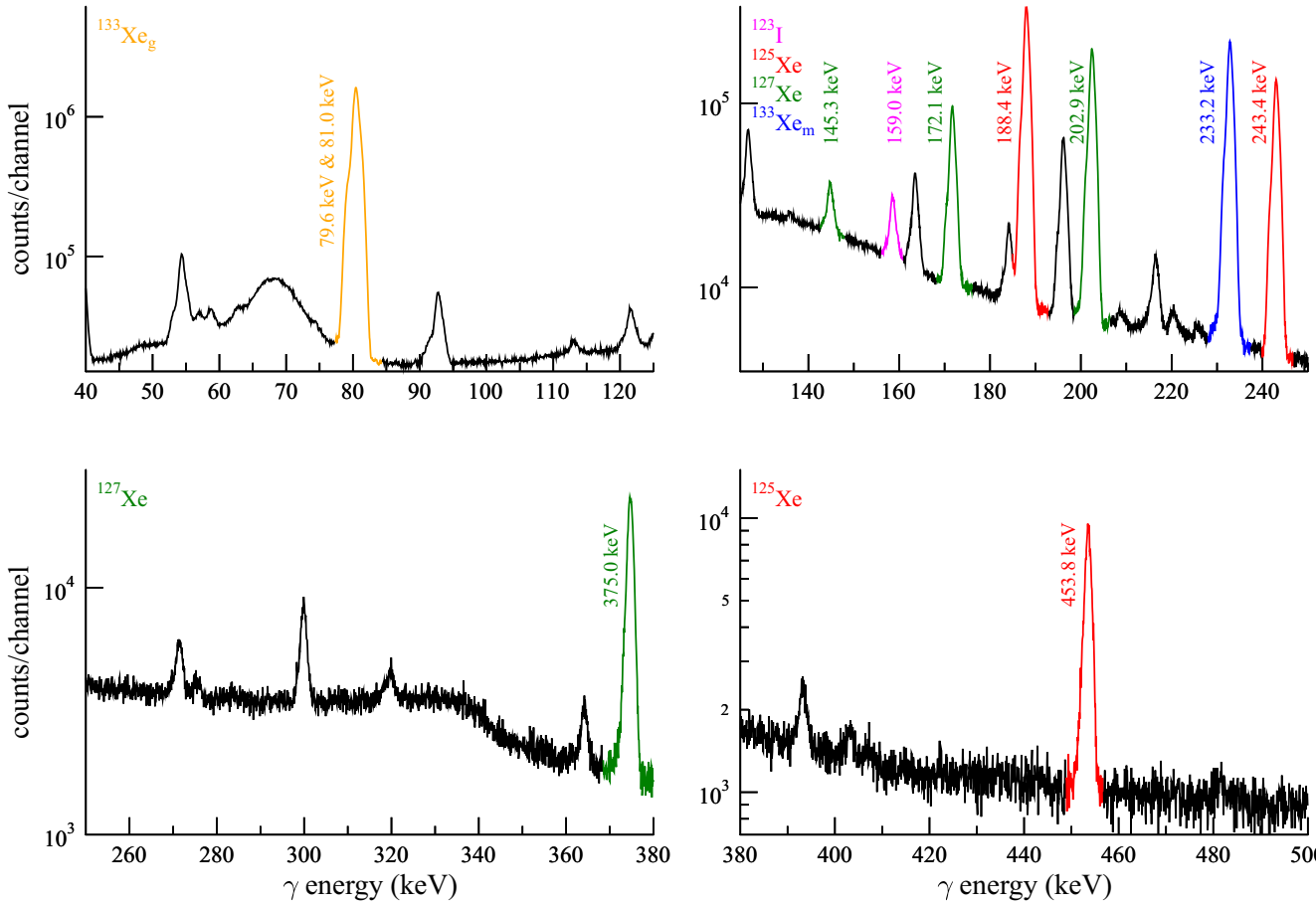

FIG. 3. γ spectrum measured with the planar detector on a target irradiated with a 16 MeV α beam. The spectrum is split into four panels with different vertical scales in order to see the relevant γ peaks. The peaks used for the analysis are labeled. The other visible peaks correspond either to beam-induced or laboratory background or weaker transitions from Xe isotopes not used for the analysis.

Here the first column gives the mean α beam energy after passing through the degrader foil. The initial α energy in this case was 11 MeV.

The second column contains the effective energies in the center-of-mass frame, which take into account the energy loss of the beam in the target layers. This energy loss, obtained with the SRIM code using the known target thicknesses, is between 80 and 125 keV. In such an energy interval the (α, n) cross sections change only moderately, but this change is not known *a priori* and varies from channel to channel. Therefore, the effective energy is simply assigned to the middle of the

TABLE III. Experimental cross section and S-factor results of the ^{122}Te (α, n) ^{125}Xe reaction. The cross section in the last row (typeset in italic) is not purely from the ^{122}Te (α, n) ^{125}Xe reaction, but has contribution from the ^{123}Te$(\alpha, 2n)$ ^{125}Xe reaction. See text for details.

E_α (MeV)	$E^{\text{eff}}_{\text{c.m.}}$ (MeV)	Cross section (mb)	S factor (10^{25} keV b)
10.0	9.612 ± 0.082	0.0172 ± 0.0033	396 ± 77
11.0	10.591 ± 0.072	0.319 ± 0.030	367 ± 35
12.0	11.563 ± 0.070	2.31 ± 0.18	200 ± 16
13.0	12.531 ± 0.071	14.0 ± 1.1	125 ± 10
14.0	13.504 ± 0.069	58.6 ± 4.5	69.3 ± 5.3
15.0	14.476 ± 0.068	149 ± 11	28.8 ± 2.2
16.0	15.446 ± 0.068	271 ± 21	10.2 ± 0.8
17.0	*16.419 ± 0.066*	*380 ± 30*	*3.23 ± 0.25*

TABLE IV. Experimental cross section and S-factor results of the ^{124}Te (α, n) ^{127}Xe reaction. The cross sections in the last three rows (typeset in italic) are not purely from the ^{124}Te (α, n) ^{127}Xe reaction, but have contribution from the ^{125}Te$(\alpha, 2n)$ ^{127}Xe reaction. See text for details.

E_α (MeV)	$E^{\text{eff}}_{\text{c.m.}}$ (MeV)	Cross section (mb)	S factor (10^{25} keV b)
10.0	9.617 ± 0.082	0.0300 ± 0.0063	689 ± 144
11.0	10.597 ± 0.072	0.369 ± 0.038	424 ± 44
12.0	11.569 ± 0.070	2.45 ± 0.22	212 ± 19
13.0	12.538 ± 0.071	15.5 ± 1.2	139 ± 11
14.0	13.511 ± 0.069	60.5 ± 4.9	71.6 ± 5.8
15.0	*14.483 ± 0.068*	*159 ± 13*	*30.7 ± 2.5*
16.0	*15.454 ± 0.068*	*365 ± 29*	*13.7 ± 1.1*
17.0	*16.428 ± 0.066*	*619 ± 50*	*5.25 ± 0.42*

TABLE V. Experimental cross section and *S*-factor results of the ^{130}Te (α, n) ^{133}Xe reaction. Partial cross sections leading to the ground and isomeric states of ^{133}Xe are listed separately as well as their sum as the total cross section. The quoted *S* factors correspond to the total cross section. See text for details.

E_α	$E^{\text{eff}}_{\text{c.m.}}$	Cross section (mb)			*S* factor
(MeV)	(MeV)	Ground state	Isomeric state	Total	(10^{25} keV b)
10.0	9.631 ± 0.082	0.0263 ± 0.0030	0.0127 ± 0.0023	0.0390 ± 0.0042	899.1 ± 97.8
11.0	10.612 ± 0.072	0.315 ± 0.030	0.143 ± 0.016	0.457 ± 0.041	526.4 ± 47.1
12.0	11.585 ± 0.070	2.42 ± 0.19	1.127 ± 0.089	3.54 ± 0.27	307.6 ± 23.8
13.0	12.556 ± 0.072	10.5 ± 0.8	6.14 ± 0.49	16.6 ± 1.3	149.5 ± 11.7
14.0	13.531 ± 0.069	26.9 ± 2.1	22.0 ± 1.7	48.9 ± 3.8	57.9 ± 4.5
15.0	14.504 ± 0.068	36.4 ± 2.8	43.3 ± 3.3	79.7 ± 6.1	15.4 ± 1.2
16.0	15.477 ± 0.068	35.6 ± 2.8	56.0 ± 4.2	91.6 ± 7.1	3.46 ± 0.27
17.0	16.451 ± 0.066	28.5 ± 2.3	49.5 ± 3.8	78.0 ± 6.0	0.66 ± 0.05

target where half of the energy loss is reached. The quoted uncertainty of the effective energies correspond to the whole α-energy range covered by the target and also takes into account the uncertainties of the primary beam energy, the target thickness and the stopping power.

The cross section values for the measured reactions are listed in the tables with their total uncertainties. These uncertainties are obtained as the quadratic sum of the following components: statistical uncertainty from the γ-spectrum analysis (always <35%, in most cases <5%) and systematic uncertainties from beam charge integration (3%), target thickness (4%), detection efficiency including geometry conversion factors (3–5%), and decay parameters (<6%). Owing to the recent high-precision measurement [22], the uncertainty of the natural Te isotopic abundances are well below 1% (including the previously poorly known ^{120}Te [21]) and are therefore negligible.

The rightmost column of the tables shows the astrophysical *S*-factor values calculated from the cross sections [1]. These *S* factors will be used in the figures in the next section dealing with the analysis of the results. The quoted *S*-factor uncertainties do not include the energy uncertainties.

Since the cross sections were measured with the activation method and natural isotopic composition targets were used, different reaction channels leading to the same produced isotope cannot be distinguished. In the studied energy range such disturbing reaction channels are the following:

(1) ^{123}Te$(\alpha, 2n)$ ^{125}Xe, leading to the same reaction product as ^{122}Te(α, n) ^{125}Xe. The threshold of this reaction is at 16.08 MeV. Therefore, it can contribute to the measured ^{125}Xe decay yield at the highest measured energy of $E_\alpha = 17$ MeV. The last row in Table III typeset in italic shows thus not the pure ^{122}Te(α, n) ^{125}Xe cross section, but the sum of the two cross sections weighted by the isotopic ratios: $\sigma(^{122}\text{Te}(\alpha, n)\,^{125}\text{Xe}) + 0.884/2.529 \times \sigma(^{123}\text{Te}(\alpha, 2n)\,^{125}\text{Xe})$.

(2) ^{125}Te$(\alpha, 2n)$ ^{127}Xe, leading to the same reaction product as ^{124}Te(α, n) ^{127}Xe. The threshold of this reaction is at 14.77 MeV. Therefore, it can contribute to the measured ^{127}Xe decay yield at the three highest measured energies of $E_\alpha = 15$, 16 and 17 MeV. The last three rows in Table IV typeset in italic show thus not the pure ^{124}Te(α, n) ^{127}Xe cross section, but the sum of the two cross sections weighted by the isotopic ratios: $\sigma(^{124}\text{Te}(\alpha, n)\,^{127}\text{Xe}) + 7.049/4.716 \times \sigma(^{125}\text{Te}(\alpha, 2n)\,^{127}\text{Xe})$.

(3) ^{123}Te (α, γ) ^{127}Xe, leading to the same reaction product as ^{124}Te(α, n) ^{127}Xe. In general, (α, γ) cross sections are much lower than (α, n) cross sections, and the natural abundance of ^{123}Te is about a factor of 5 smaller than the abundance of ^{124}Te. Using TALYS default parameters for the γ-strength function and the level density, the contribution of the ^{123}Te(α, γ) ^{127}Xe reaction to the ^{127}Xe yield is about 0.1% at the lowest energy of the present study and even lower at higher energies. We have investigated the range of calculated (α, γ) cross sections for all γ-strength functions and level densities which are available in TALYS. For practically all combinations the yield from ^{123}Te(α, γ) ^{127}Xe remains far below 1%, and even using the highest calculated ^{123}Te(α, γ) ^{127}Xe cross section contributes only by about 2.5% at the lowest energy and less than 0.2% at the highest energy of the present study. Thus, the contribution of the ^{123}Te(α, γ) ^{127}Xe reaction to the ^{127}Xe yield is by far within the experimental uncertainties and can be safely neglected.

The effect of the $(\alpha, 2n)$ reaction channels will be taken into account in the theoretical analysis in the next section.

IV. THEORETICAL ANALYSIS

A. General remarks

A major goal of the present work is the study of α-nucleus optical model potentials (AOMPs). As already pointed out in the Introduction, angular distributions of elastic scattering are the basic building block for the determination of the AOMP. More than fifty years ago, McFadden and Satchler (MCF) determined a simple four-parameter AOMP [10]: The depths V_0 and W_0, the radius R_0 (with $R = R_0 \times A_T^{1/3}$), and the diffuseness a of the real and imaginary parts of a volume Woods-Saxon (WS) potential were adjusted to fit a wide range of elastic scattering angular distributions around

25 MeV. Later, additional cross section data from α-induced reactions like (α,γ), (α,n), and (α,p) were included in the analysis, and the real part of the potential was replaced by a folding potential [36]. Three different versions of this AOMP of Demetriou *et al.* (in the following, DEM) were provided which use different shapes of the imaginary part and a dispersive coupling of the real and imaginary parts in the third version (DEM3). Avrigeanu *et al.* (in the following: AVR) [37,38] went back to a WS shaped AOMP where many parameters were adjusted to match a wide range of available α-induced (α,X) data. The benefit of the DEM and AVR approaches is a better reproduction of the (α,X) data when compared to the MCF approach, in particular towards lower energies below the Coulomb barrier, which is the astrophysically relevant energy region. Disadvantages are the increasing number of free parameters and a strong sensitivity to the chosen (α,X) data. In detail, the latter sensitivity to a particular data set for ^{120}Te$(\alpha,n)^{123}$Xe by Palumbo *et al.* [39] will be illustrated below.

In the recent years, it was noticed that the calculation of (α,X) reaction cross sections at very low energies depends very sensitively on the strength of the imaginary part of the AOMP at large radii (far beyond the colliding nuclei) which is not at all constrained by elastic scattering and only poorly constrained by (α,X) data. Therefore, a new AOMP was introduced which is based purely on the barrier transmission model [40]. The underlying real part of the AOMP was taken from the folding approach. The few parameters were adjusted—in a similar way as in the MCF potential—to elastic scattering angular distributions at low energies [41]. As the few parameters of this so-called Atomki-V2 AOMP are fully fixed to elastic scattering, the Atomki-V2 AOMP allows the robust prediction of (α,X) cross sections without further parameter adjustment. It was found in [40] that these predictions from the Atomki-V2 AOMP are robust within less than a factor of 2 for all α-induced (α,X) cross sections of heavy target nuclei at low energies. This is further confirmed by recent measurements [15,18,20,42]. A database of astrophysical (α,X) reaction rates from the Atomki-V2 AOMP is already provided in [43].

B. Statistical model and ingredients

The following calculations of the (α,n) reaction cross sections are based on the statistical model [2]. In a schematic notation, the cross section of an α-induced (α,X) reaction is given by

$$\sigma(\alpha,X) \sim \frac{T_{\alpha,0}T_X}{\sum_{T_i}} = T_{\alpha,0} \times b_X \qquad (1)$$

with the transmission coefficients $T_{\alpha,0}$ of the incoming αparticle, T_i for the outgoing particles ($i=\gamma,p,n,\alpha,2n$, etc.), and the branching ratio $b_X = T_X/\sum_i T_i$ for the branching into the X channel. Usually, the transmissions T_i are calculated from optical model potentials for the particle channels and from the γ-ray strength function for the (α,γ) capture channel. All T_i depend implicitly on the chosen level densities for the residual nuclei. For further details see, e.g., [3,44]. The TALYS code [45,46] was used for the following calculations.

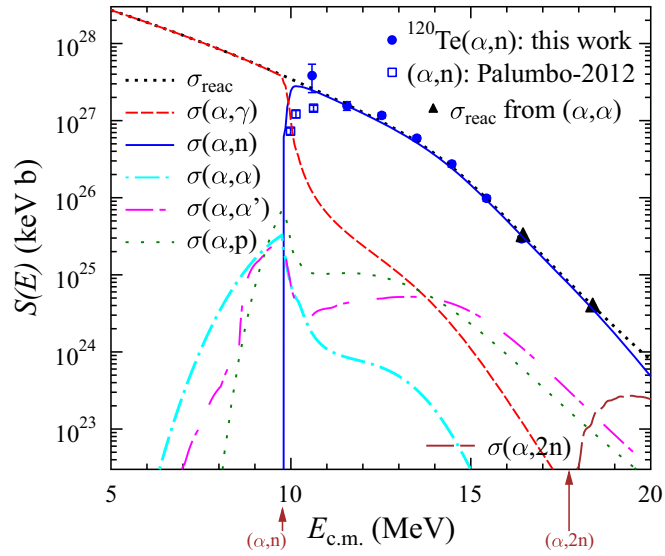

FIG. 4. Decomposition of the total reaction cross section σ_{reac} (black dotted) of ^{120}Te + α into the contributions of the different (α,X) channels. The (α,γ) channel (red dashed) is dominating below the (α,n) threshold. The (α,n) channel (blue) becomes dominating within about 1 MeV above the (α,n) threshold. Only at high energies around 20 MeV does the contribution of the $(\alpha,2n)$ channel (brown long-dashed) contribute significantly. The contributions of the other open channels remain negligible for all energies under study. The vertical arrows show the (α,n) and $(\alpha,2n)$ thresholds. All cross sections have been converted to astrophysical S factors.

For heavy target nuclei, there are common properties for the branching $b_X = T_X/\sum_i T_i$ in Eq. (1). At low energies below the (α,n) threshold, the transmissions for charged particles are strongly suppressed by the Coulomb barrier, and thus the dominating transmission is T_γ for the photon channel. This leads to $b_\gamma \approx 1$ below the (α,n) threshold. Above the (α,n) threshold, neutron emission is dominating which leads to $b_n \approx 1$ already close above the (α,n) threshold. At high energies above the $(\alpha,2n)$ threshold, the (α,n) and $(\alpha,2n)$ channels compete, leading to $b_n + b_{nn} \approx 1$. As soon as $b_X \approx 1$ is found for a particular channel, the corresponding (α,X) cross section depends essentially only on $T_{\alpha,0}$ which in turn only depends on the chosen AOMP but not on the other ingredients of the statistical model. Hence we focus on the role of the AOMP in the subsequent analysis whereas the other ingredients of the statistical model play only a very minor role. This discussion is extended at the end of Sec. IV D.

The above considerations on the branching b_X are visualized for ^{120}Te + α in Fig. 4. For better visibility, all cross sections are converted to astrophysical S factors which show only a moderate energy dependence (compared to the steeper energy dependence of the underlying cross sections).

C. Additional data from elastic scattering

As pointed out above, the experimental (α,n) cross sections provide an excellent constraint for the AOMP because

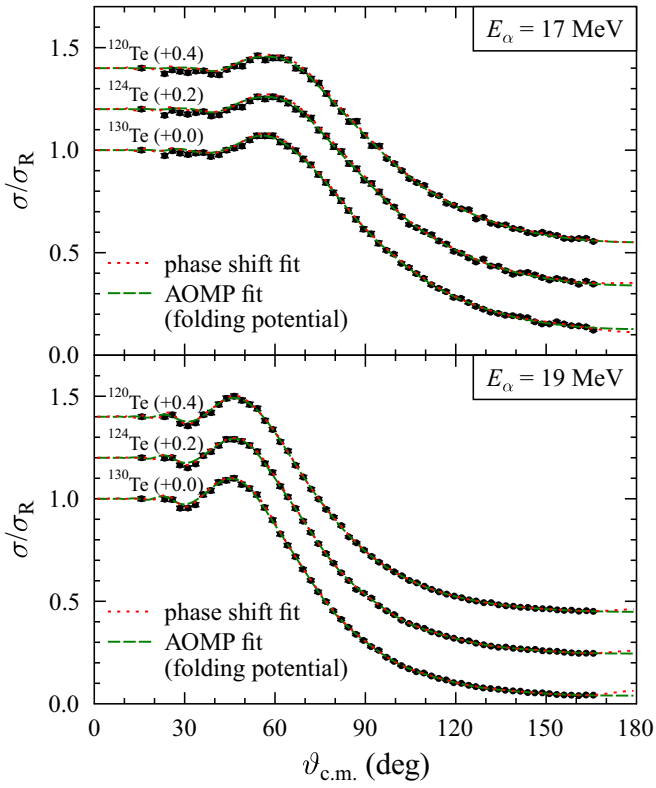

FIG. 5. Elastic scattering angular distributions for ^{120}Te$(\alpha,\alpha)^{120}$Te, ^{124}Te$(\alpha,\alpha)^{124}$Te, and ^{130}Te$(\alpha,\alpha)^{130}$Te at 17 MeV (upper part) and 19 MeV (lower part): The experimental data of [47] are well reproduced by phase shift fits (red dotted) and AOMP fits (green dashed). Both lines overlap almost fully; the differences are hardly visible. The resulting total reaction cross sections σ_{reac} are listed in Table VI. For further explanations see text.

the calculated (α, n) cross sections are mainly sensitive to the AOMP only. At higher energies, the total reaction cross section σ_{reac} of α-induced reactions can also be used to test the AOMP. σ_{reac} is derived from the analysis of the elastic scattering angular distributions. Full angular distributions at low energies were measured by Palumbo *et al.* [47], but unfortunately σ_{reac} was not determined in [47]. Hence we have reanalyzed the data of [47] for ^{120}Te, ^{124}Te, and ^{130}Te below 20 MeV using either phase shift fits or AOMP fits. Figure 5 shows that the (α, α) angular distributions of Palumbo *et al.* [47] at 17 and 19 MeV are very well reproduced by both approaches. The phase shift fits (red dotted lines in Fig. 5) achieve $\chi^2/F \lesssim 1.0$, and the AOMP fits (based on a folding potential in the real part and a surface Woods-Saxon imaginary part) show slightly higher $\chi^2/F \approx 1.0$–1.5 (green dashed lines in Fig. 5).

TABLE VI. Total reaction cross sections σ_{reac} for various tellurium isotopes, derived from elastic scattering [47]. One independent data point for ^{124}Te at 19.3 MeV [48] confirms the present results.

Isotope	E_α (MeV)	σ_{reac} (mb)
^{120}Te	17.0	397±20
^{120}Te	19.0	648±32
^{124}Te	17.0	407±20
^{124}Te	19.0	673±34
^{124}Te	19.3	660 [48]
^{130}Te	17.0	444±22
^{130}Te	19.0	711±36

The resulting σ_{reac} are calculated from the reflexion coefficients η_L of the phase shift fits and of the AOMP fits. The σ_{reac} from both approaches agree within a few percent in all cases under study. The average of both approaches is finally given as σ_{reac} in Table VI. The analysis benefits from the fact that the angular distributions in [47] cover the almost full angular range with small uncertainties.

For comparison, we include another data point for σ_{reac} of ^{124}Te$(\alpha,\alpha)^{124}$Te from the data of [48] at 19.3 MeV. A calculation of the total reaction cross section σ_{reac} from the optical model parameters in Table I of [48] results in $\sigma_{reac} = 969$ mb, i.e., significantly above the corresponding σ_{reac} derived from the Palumbo *et al.* data [47]. However, the calculated angular distribution from these parameters in Table I of [48] does not match the experimental data in their Fig. 2. A much better agreement is obtained when the radius parameter r_0 of 1.395 fm is replaced by 1.24 fm. The latter value is given in several other lines in Table I of [48]; this points to a simple typo in Table I. Using $r_0 = 1.24$ fm, we find $\sigma_{reac} = 660$ mb, consistent with the results by Palumbo *et al.*; hence, this value is listed in Table VI. An attempt to refit the angular distribution of [48] is hampered by the fact that the data at EXFOR had to be redigitized from Fig. 2 which results in additional uncertainties. Furthermore, the data in Fig. 2 of [48] do not show experimental uncertainties. A refit of the EXFOR data, assuming a constant uncertainty of 5% for all data points, leads to slightly higher σ_{reac} between about 700 and 770 mb. The larger scatter of the derived σ_{reac} in the fits results from the smaller angular range and the lower number of experimental data points which do not allow a phase shift analysis. Overall, despite the above uncertainties under discussion, the data at 19.3 MeV by [48] confirm the consistency of the σ_{reac} from the experimental scattering data of [47] within the given uncertainties.

Note that the data points for the total reaction cross section σ_{reac} from elastic scattering at 17 MeV by Palumbo *et al.* [47] are shown in all figures for ^{120}Te, ^{124}Te, and ^{130}Te as black triangles, whereas the 19 MeV data are above the energy range of the present (α, n) data and thus outside the chosen scale of some figures. For clarification we point out that the three data points for the ^{120}Te$(\alpha, n)^{123}$Xe reaction by Palumbo *et al.* [39] are shown in the respective figures for ^{120}Te by blue squares.

D. Further technical remarks

The calculations in the present study are mainly done with version 1.80 of TALYS [45,46]. This choice is motivated by a poorly documented modification of the AOMPs by Demetriou *et al.* [36] in later versions. For explanation, we present the ratio between TALYS 1.80 and TALYS 1.96 for the calculated

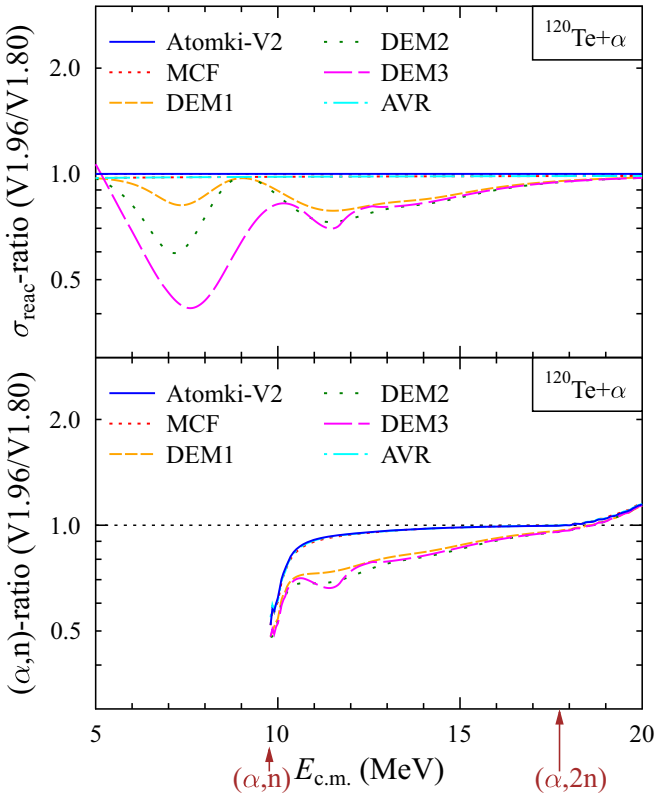

FIG. 6. Comparison of the TALYS versions 1.80 and 1.96 for the total reaction cross section σ_{reac} (upper) and the (α, n) cross section (lower) for the example of ^{120}Te. For further discussion see text.

total reaction cross section σ_{reac} and for the (α, n) cross section in Fig. 6.

The total reaction cross section σ_{reac} depends only on the AOMP, and thus the results from different TALYS versions should be identical. As expected, the σ_{reac} are indeed identical for the MCF, the AVR, and the Atomki-V2 AOMPs; see Fig. 6, upper part. However, the ratio deviates significantly from unity for the DEM1, DEM2, and DEM3 AOMPs.

It has been pointed out by the TALYS authors [49] that a modification of the DEM1, DEM2, and DEM3 AOMPs was implemented in TALYS version 1.96 which is based on further studies of α-induced reaction cross sections by Demetriou. Unfortunately, this modification was not yet listed in the detailed "Log file of changes" at the end of the TALYS manual; this will change in the next TALYS release. At present, the explanation can only be found as a comment in the TALYS source code "*foldalpha.f*": *"csg Correction of the radius dependence of the real part after an analysis of the (a,g) and (a,n) data of deformed nuclei : 27/4/2018 (Brussels) increase of rva by 3% for deformed nuclei but only below typically 18 MeV"*. The source code shows that the correction of the radius depends on the deformation parameter β_2. In the case of ^{120}Te, the negative β_2 in TALYS leads to a decrease of the radius of the real potential (the statement in the comment is only valid for $\beta_2 > 0$). A reduced radius of the attractive real part of the AOMP leads to an effective increase of the Coulomb barrier and thus to lower total reaction cross sections σ_{reac} (as visible in the upper part of Fig. 6). We prefer to use the original DEM1, DEM2, and DEM3 AOMPs without the undocumented modification in TALYS 1.96, and thus we use TALYS 1.80 in the following analysis of the (α, n) cross sections.

For completeness we note that there is another difference between TALYS 1.80 and TALYS 1.96 which becomes visible in the (α, n) cross sections. The default γ-strength function (GSF) was changed, which leads to a larger GSF in TALYS 1.96. As a consequence, close above the (α, n) threshold the (α, γ) contribution is larger, which in turn leads to smaller (α, n) cross sections. This effect is mostly visible in the first MeV above the (α, n) threshold, but remains within about 10% at higher energies. This will be discussed further in the analysis of the ^{120}Te$(\alpha, n)^{123}$Xe reaction in Sec. IV E 1. As expected, both TALYS versions in use provide identical results as soon as the same GSF is selected.

The results from the different default options for the GSF in the TALYS versions 1.80 and 1.96 are shown in Fig. 7 for the ^{120}Te$(\alpha, \gamma)^{124}$Xe reaction. This comparison can be used to assess the relevance of the GSF for the present analysis.

Below the (α, n) threshold, the only open channels are (α, α) elastic and inelastic scattering and (α, γ) capture. Because of the high Coulomb barrier, the transmission into the α channel is much smaller than the transmission into the γ channel: $T_\alpha \ll T_\gamma$. This leads to a branching $b_\gamma \approx 1$ in Eq. (1) and thus $\sigma(\alpha, \gamma) \approx \sigma_{reac}$. This holds for all AOMPs under study and for the lower GSF in TALYS 1.80 as well as for the higher GSF in TALYS 1.96 (see upper and middle parts of Fig. 7).

Above the (α, n) threshold, the (α, n) channel dominates, and thus the branching b_γ in Eq. (1) becomes approximately $b_\gamma \approx T_\gamma/(T_\gamma + T_n) \approx T_\gamma/T_n$ at higher energies. In practice, b_γ is of the order of a few per cent close above the (α, n) threshold and decreases to about 10^{-3} at higher energies (see Fig. 7, upper and middle parts). The GSF is about a factor of 3 larger in TALYS 1.96, as can be seen at the higher energies in Fig. 7, lower part. The same factor is found for the branching ratios b_γ. A further enhancement of the GSF (exceeding a factor of th3ree between the different GSFs in TALYS 1.80 and 1.96) will lead to further increasing b_γ and simultaneous decrease of b_n and the (α, n) cross section. However, a reduction of the GSF will have only very minor influence because a reduction of b_γ from, e.g., 10^{-3} to 10^{-4} will enhance the neutron branching $b_n \approx 1 - b_\gamma$ only from 0.999 to 0.9999, which is less than 0.1%.

Finally we note an interesting detail: The increased GSF in TALYS 1.96 is responsible for the increase of the ratio of (α, n) cross sections above the $(\alpha, 2n)$ threshold; see Fig. 6, lower part. The increased GSF favors the γ decay of highly excited ^{123}Xe residual nuclei and thus reduces the probability of emission of a second neutron and the $(\alpha, 2n)$ cross section.

E. Comparison between experimental data and theory

1. ^{120}Te (α, n) ^{123}Xe

Figure 8 compares the experimental (α, n) data from this work and from Palumbo *et al.* [39] to TALYS calculations using different AOMPs. It is obvious that all AOMPs except

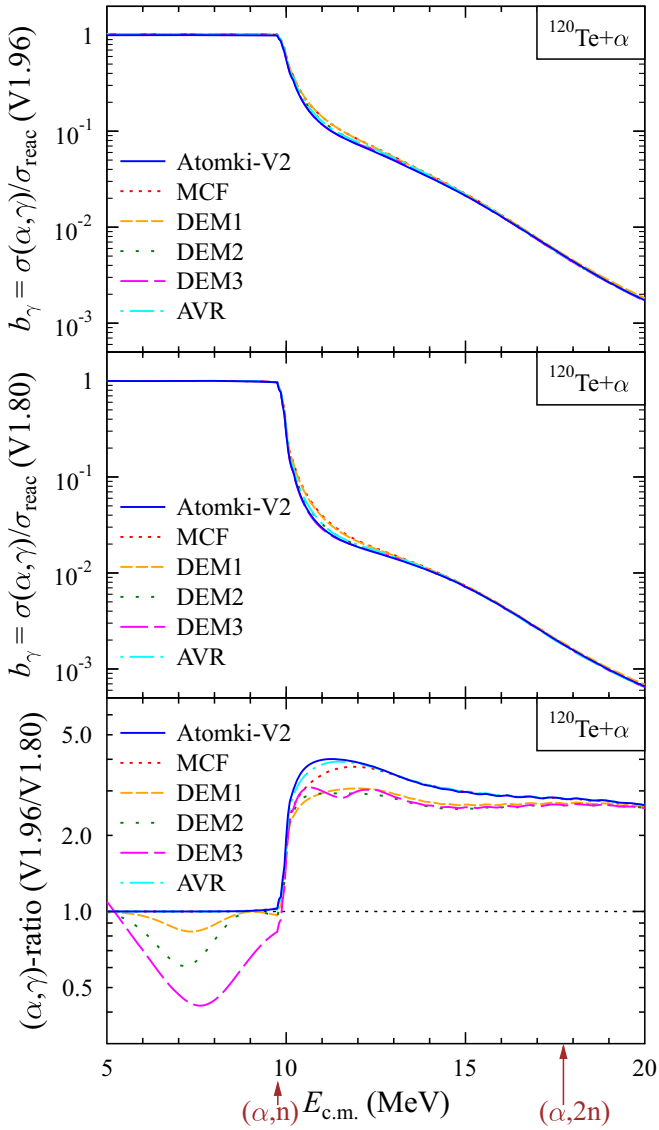

FIG. 7. Comparison of the TALYS versions 1.80 and 1.96 for the ^{120}Te$(\alpha,\gamma)^{124}$Xe cross section and the relevance of the GSF: ratio of the (α,γ) cross sections of TALYS versions 1.96 and 1.80 for different AOMPs (lower part); ratio of the (α,γ) cross section to the total cross section σ_{reac} for TALYS version 1.80 (middle part); same, but for TALYS version 1.96 (upper part). For further discussion see text.

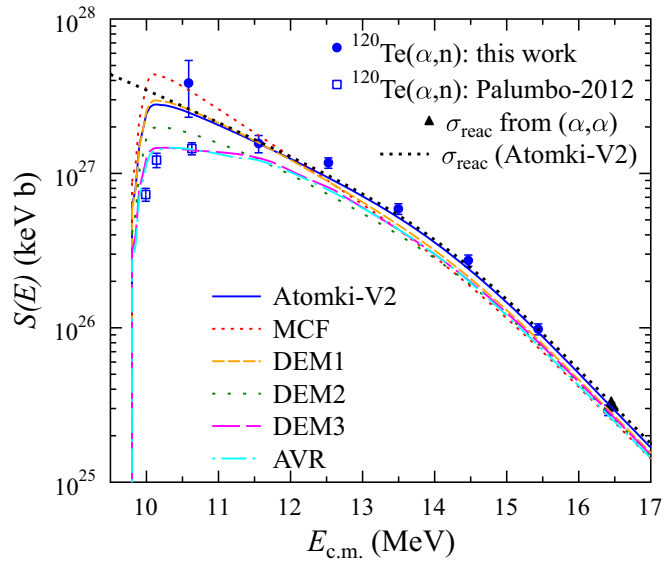

FIG. 8. Reaction cross section of the ^{120}Te$(\alpha,n)^{123}$Xe reaction (shown as astrophysical S factor): comparison of the experimental data to TALYS calculations using different AOMPs. In addition, the total reaction cross section σ_{reac} from the Atomki-V2 AOMP (black dashed) is compared to σ_{reac} from elastic scattering (black triangle, see Table VI). The $(\alpha,2n)$ threshold located at $E_{c.m.} = 17.725$ MeV is outside the energy range of the figure.

the Atomki-V2 AOMP underestimate the experimental data above 11 MeV where the (α,n) cross sections are mainly sensitive to the AOMP. There is excellent agreement between the total cross section σ_{reac} from elastic scattering and the (α,n) cross section from this work at $E_{c.m.} \approx 16.4$ MeV (note that both data points, black triangle and blue circle, are almost hidden behind the various lines from the AOMP calculations).

There is some tension among the three low-energy data points by Palumbo *et al.* and our lowest data point around 11 MeV. Unfortunately, there is no overlap region where both data sets provide (α,n) cross sections with small uncertainties. Thus, the (α,n) cross section near the (α,n) threshold remains somewhat uncertain. An improvement of the present experiment requires enriched targets, which were also used in the Palumbo *et al.* experiment.

The standard calculation with the Atomki-V2 AOMP in TALYS 1.80 fits the present data over the full energy range, favoring the high cross section at the lowest energy of the present experiment. However, following the findings in Sec. IV D, the (α,n) cross section may be reduced by an enhanced (α,γ) contribution. As an example, we show in Fig. 9 that an additional pygmy dipole strength enhances the (α,γ) cross section in such a way that the low (α,n) cross sections of Palumbo *et al.* close above the threshold are nicely reproduced. But such an enhanced (α,γ) contribution would slightly reduce the (α,n) cross sections up to about 15 MeV. A simultaneous fit of the low (α,n) data by Palumbo *et al.* close above the threshold and the present data over the full energy range is practically impossible without very special adjustments of the GSFs and the level densities which affect the branching between the (α,γ) and (α,n) channels.

The AVR AOMP was adjusted—among many others—to the low (α,n) cross sections of Palumbo *et al.*. Obviously, this had lead to parameters of the AOMP which underestimate the (α,n) cross sections at higher energies. Similar underestimations of the (α,n) cross sections are found for the other tellurium isotopes under study in the present work (see subsequent sections).

The DEM1, DEM2, and DEM3 AOMPs were derived before the Palumbo *et al.* experiment. Thus, there is no obvious reason for the overall underestimation of the (α,n) cross section which holds also for the other tellurium isotopes under study (see subsequent sections). We note that the underestimation increases further when the undocumented modification

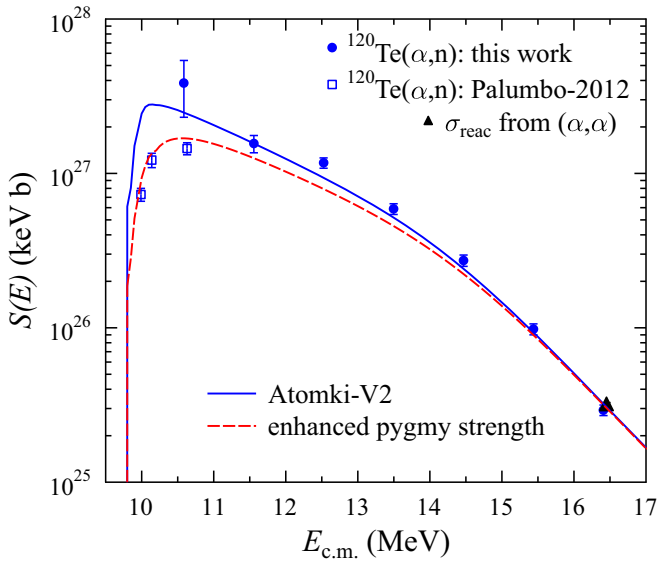

FIG. 9. Reaction cross section of the ^{120}Te$(\alpha, n)^{123}$Xe reaction (shown as astrophysical S factor) from the Atomki-V2 AOMP with the default GSF of TALYS 1.80 (blue) and with an additional pygmy dipole strength at low energies (red dashed). For further discussion see text.

of the DEM1, DEM2, and DEM3 AOMPs in TALYS 1.96 is applied because this modification reduces the (α, n) cross sections by about 10–30% in the energy range of the present study.

2. ^{122}Te (α, n) ^{125}Xe

The results for ^{122}Te$(\alpha, n)^{125}$Xe are shown in Fig. 10. Similarly to ^{120}Te$(\alpha, n)^{123}$Xe in the previous section, the

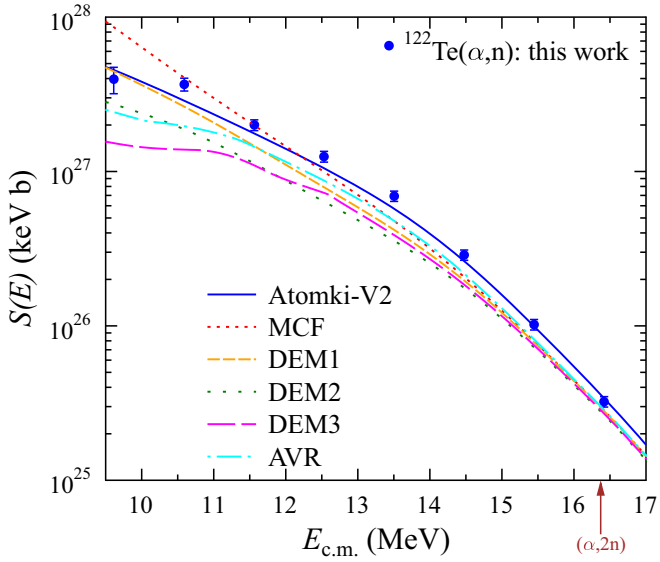

FIG. 10. Reaction cross section of the ^{122}Te$(\alpha, n)^{125}$Xe reaction (shown as astrophysical S factor): comparison of the experimental data to TALYS calculations using different AOMPs. The $(\alpha, 2n)$ threshold is indicated by a vertical arrow.

new experimental data are well reproduced by the Atomki-V2 AOMP. The DEM1, DEM2, DEM3, and AVR AOMPs underestimate the new experimental data over the full energy range. The MCF AOMP shows a much steeper energy dependence than all other AOMPs, leading to an overestimation of the (α, n) cross section towards the lowest energies. This is a well-known finding for the MCF AOMP for heavy target nuclei.

The new data point at the highest energy may have received a minor contribution from the ^{123}Te$(\alpha, 2n)^{125}$Xe reaction. We estimate this contribution to be about 5%, i.e., within the given uncertainties. No correction is applied here. Further information on the contributions of the $(\alpha, 2n)$ reaction can be found in the subsequent Sec. IV E 3 on the ^{124}Te$(\alpha, n)^{127}$Xe reaction.

The (α, n) threshold of the ^{122}Te$(\alpha, n)^{125}$Xe reaction is located at 8.77 MeV. Our lowest data point is located about 1 MeV above the (α, n) threshold. Unfortunately, the new experimental data do not cover the first MeV above the (α, n) threshold, which would allow a better comparison with the ^{120}Te$(\alpha, n)^{123}$Xe reaction close above the threshold with the discrepant data by Palumbo *et al.* and from the present study.

Again unfortunately, elastic scattering angular distributions are not available for ^{122}Te. Thus, a comparison of the total reaction cross section σ_{reac} from elastic scattering to the (α, n) data from the present experiment is not possible. Furthermore, the EXFOR database does not show any cross sections for the ^{122}Te$(\alpha, n)^{125}$Xe reaction in the literature.

3. ^{124}Te (α, n) ^{127}Xe

In general, the results for the ^{124}Te$(\alpha, n)^{127}$Xe reaction in Fig. 11 are similar as in the two previous sections. The Atomki-V2 AOMP provides a good description of the new experimental data although the calculation is slightly lower than the experimental data. The DEM1, DEM2, DEM3, and AVR AOMPs also underestimate the experimental data with a somewhat larger deviation than the Atomki-V2 AOMP. The MCF AOMP shows a stronger energy dependence than the other AOMPs.

Along the tellurium isotopic chain, the Q-value of the (α, n) reaction becomes less negative with increasing neutron number. This holds also for the $(\alpha, 2n)$ reactions. A first consequence is that the difference between the total cross section σ_{reac} (black dashed line in Fig. 11) and the (α, n) cross section (blue line) becomes clearly visible around 16 MeV which is about 1 MeV above the $(\alpha, 2n)$ threshold for ^{124}Te.

A second consequence of the lowering of the Q-values is the fact that a significant contribution of the $(\alpha, 2n)$ reaction on the neighboring $N + 1$ isotope ^{125}Te has to be expected for the ^{127}Xe yield at higher energies. As discussed in Sec. III D, it is not possible to disentangle the contributions from the ^{124}Te$(\alpha, n)^{127}$Xe and ^{125}Te$(\alpha, 2n)^{127}$Xe reactions in the present activation experiment. Assigning the total ^{127}Xe yield to the ^{124}Te$(\alpha, n)^{127}$Xe reaction overestimates the real (α, n) cross section. This becomes nicely visible for the two data points at 15.5 and 16.4 MeV (shown as red circles in Fig. 11). In particular, the data point at 16.4 MeV even exceeds the total cross section σ_{reac} from elastic scattering

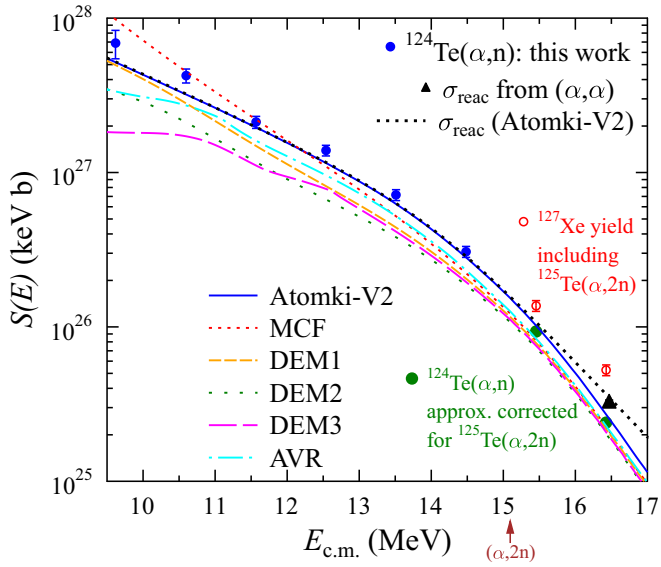

FIG. 11. Reaction cross section of the ^{124}Te$(\alpha, n)^{127}$Xe reaction (shown as astrophysical S factor): comparison of the experimental data to TALYS calculations using different AOMPs. In addition, the total reaction cross section σ_{reac} from the Atomki-V2 AOMP (black dashed) is compared to σ_{reac} from elastic scattering (black triangle, see Table VI). The $(\alpha, 2n)$ threshold is indicated by a vertical arrow. The contribution of the ^{125}Te$(\alpha, 2n)^{127}$Xe reaction is explained in the text (discussion of the red and green data points).

which is impossible. The σ_{reac} from elastic scattering can be considered as very reliable because there is an independent confirmation for ^{124}Te in [48] (see also Table VI).

For a rough estimate, we have calculated the expected yields for the ^{124}Te$(\alpha, n)^{127}$Xe and ^{125}Te$(\alpha, 2n)^{127}$Xe reactions in a natural target using TALYS 1.80 in combination with the Atomki-V2 AOMP which does a good job in general for the tellurium isotopes. This leads to a correction factor of 1/1.46 (1/2.19) at 15.5 (16.4) MeV. The correction is less than 1% for the next data point at $E_{c.m.} \approx 14.5$ MeV. The resulting cross sections for the ^{124}Te$(\alpha, n)^{127}$Xe reaction (after correction for ^{125}Te$(\alpha, 2n)^{127}$Xe) are shown as full green circles in Fig. 11. It is difficult to estimate the uncertainty of the correction. From the results for ^{130}Te (see next Sec. IV E 4) one may conclude that such a theoretical correction is slightly too strong because the ^{130}Te$(\alpha, 2n)^{128}$Xe cross section is slightly overestimated. Nevertheless, the corrected data point at 16.4 MeV is located below the total cross section σ_{reac} from elastic scattering and thus not in contradiction to σ_{reac}.

4. ^{130}Te (α, n) ^{133}Xe

The results for ^{130}Te$(\alpha, n)^{133}$Xe are shown in Fig. 12. The first excited state in ^{133}Xe at $E^* = 233$ keV with $J^\pi = 11/2^-$ is a low-lying isomer with a half-life of 2.20 days. The $3/2^+$ ground state has a longer half-life of 5.25 days. The activation yields have been determined separately, leading to a threefold Fig. 12 with the ground state contribution (upper part), the isomer contribution (middle part), and the total (α, n) cross section from the sum of the ground state plus isomer contributions (lower part).

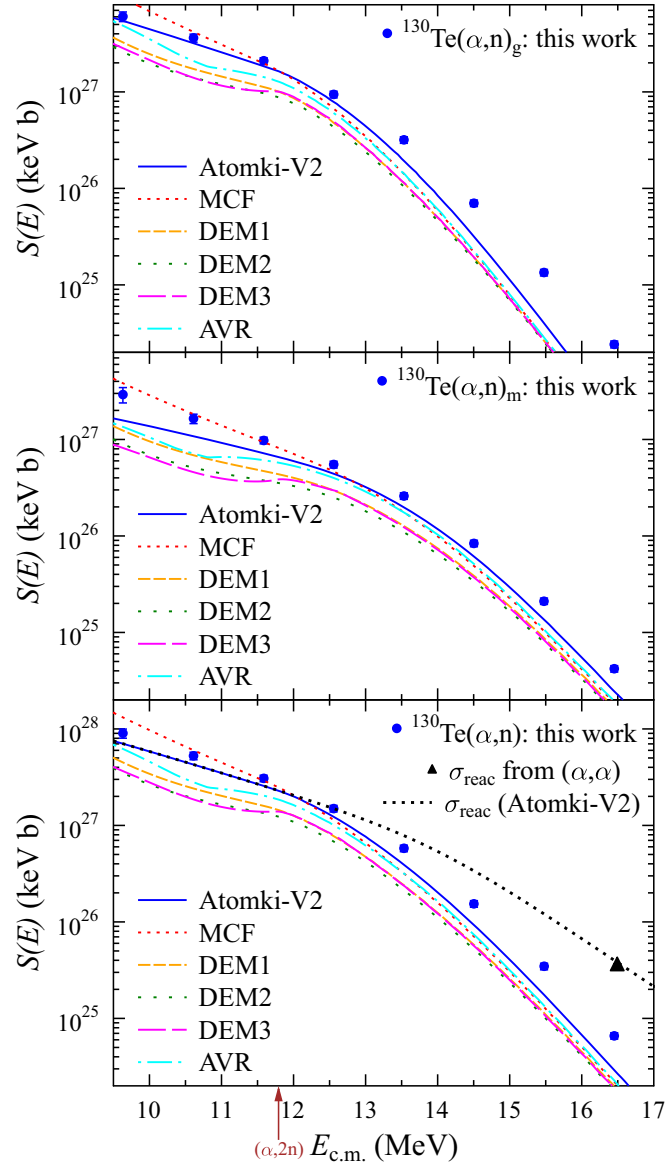

FIG. 12. Reaction cross section of the ^{130}Te$(\alpha, n)^{133}$Xe reaction (shown as astrophysical S factor): comparison of the experimental data to TALYS calculations using different AOMPs. In addition, the total reaction cross section σ_{reac} from the Atomki-V2 AOMP (black dashed) is compared to σ_{reac} from elastic scattering (black triangle, see Table VI). The lower (middle, upper) part shows the total (α, n) (isomer, ground state) cross section. The $(\alpha, 2n)$ threshold is indicated by a vertical arrow.

Let us first focus on the total (α, n) cross section in the lower part of Fig. 12. Similar to all previous cases, it is found that the DEM1, DEM2, DEM3, and AVR AOMPs show slightly lower cross sections than the Atomki-V2 AOMP. However, contrary to the previous cases, also the Atomki-V2 AOMP underestimates the experimental (α, n) data significantly. At first view, this might be misunderstood as a failure of all AOMPs. But this is not the case. The total cross section σ_{reac} from elastic scattering at 16.5 MeV clearly shows that the Atomki-V2 AOMP predicts the total cross section

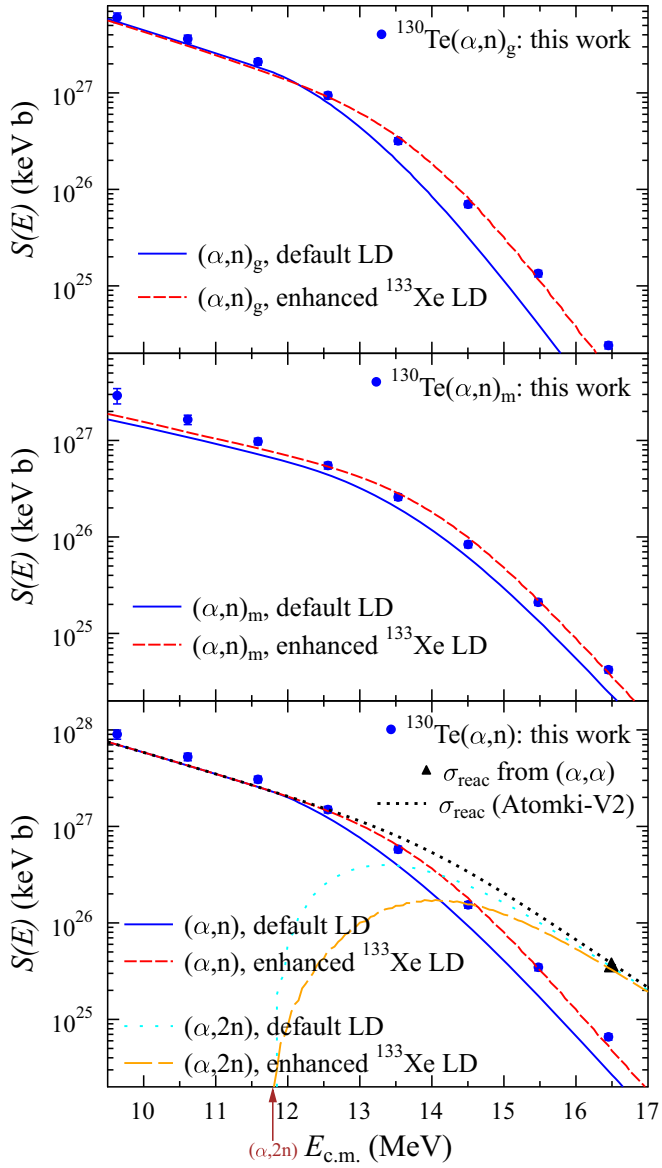

FIG. 13. Reaction cross section of the ^{130}Te$(\alpha, n)^{133}$Xe reaction (shown as astrophysical S factor): default TALYS level density (blue and light blue) vs enhanced level density for ^{133}Xe (red and orange). All calculations are based on the Atomki-V2 AOMP. For further discussion see text.

correctly. Thus, the deviation between the calculated and experimental (α, n) cross sections is not related to the AOMP, but instead indicates an overestimation of the $(\alpha, 2n)$ cross section and related underestimation of the (α, n) cross section. Note that the summed branchings of the (α, n) and $(\alpha, 2n)$ channels are $b_n + b_{2n} \approx 1$; the contributions from other channels are practically negligible above the (α, n) threshold (see also the discussion of Fig. 4 for the example of ^{120}Te).

An artificial increase of the level density (LD) in ^{133}Xe enhances the contribution of the (α, n) cross section and decreases the $(\alpha, 2n)$ cross section. This is illustrated in Fig. 13. As the total reaction cross section σ_{reac} depends only on the AOMP (but not on the chosen LD of ^{133}Xe), σ_{reac} is not affected and still reproduces the data point from elastic scattering at 16.5 MeV. At energies below the $(\alpha, 2n)$ threshold, the enhanced LD of ^{133}Xe has also no impact because the branching b_n to the (α, n) channel is anyway close to unity. Only above the $(\alpha, 2n)$ threshold does the enhanced LD of ^{133}Xe increase the (α, n) cross section and reduce the contribution of the $(\alpha, 2n)$ channel.

An even stronger increase of the LD of ^{133}Xe could also lead to a good description of the (α, n) cross sections using other AOMPs. However, the underestimation of the total cross section σ_{reac} at 16.5 MeV from elastic scattering would persist for the other AOMPs.

The total ^{130}Te$(\alpha, n)^{133}$Xe cross section is composed of the ground state contribution and the isomer contribution. The branching between these channels depends on γ-ray cascades in the residual nucleus ^{133}Xe and is practically independent of the AOMP. The upper parts of Figs. 12 and 13 show that the branching is roughly reproduced by the calculations, with a trend to underestimate the isomer contribution towards lower energies. This trend is slightly improved when the enhanced level density of ^{133}Xe is used which is required to fit the total (α, n) cross section (see Fig. 13).

We have decided to include only our new data points in Figs. 12 and 13. Several earlier data sets [50–52] are available for α-induced reactions on ^{130}Te. However, all experiments used much higher energies of the α projectiles in combination with a stacked-target technique. This typically leads to a relatively broad energy distribution at the lowest energies with significant uncertainties from the thickness and homogeneity of the targets and of the degrader foils. For completeness we show the full available data in Fig. 14. Because of the huge scatter of the experimental data, a much larger scale is required here, but still some data are not included in the chosen scale. Most of the data from [50–52] are located outside of Figs. 12 and 13. For better readability, we show only one line with a calculation; here we choose the Atomki-V2 AOMP in combination with the enhanced ^{133}Xe LD from Fig. 13 which fits our new experimental data (lightblue dashed line). Unfortunately, it must be concluded that the low-energy data from the stacked-foil experiments do not provide further insight because of the huge scatter of the data, reaching several orders of magnitude in particular towards the lowest energies, and thus by far exceeding the claimed error bars.

For completeness we note that Kirov *et al.* [50] also provide the cross section of the ^{130}Te$(\alpha, p)^{133}$I reaction. Figure 14 shows that the (α, n) data by Kirov *et al.* at low energies are much lower than our new data and all other available data sets. This leads to some doubts on these data, and we do not include the (α, p) data of Kirov *et al.* in the present analysis. Furthermore, the (α, p) cross section depends on the combination of many ingredients of the statistical model, but does not constrain the AOMP directly.

F. Discussion

It is obvious from Figs. 8, 10–12 that the deviations between the new experimental data and the calculations from various AOMPs remains limited within a factor of about $2 - 3$. Huge deviations, reaching orders of magnitude, as e.g.

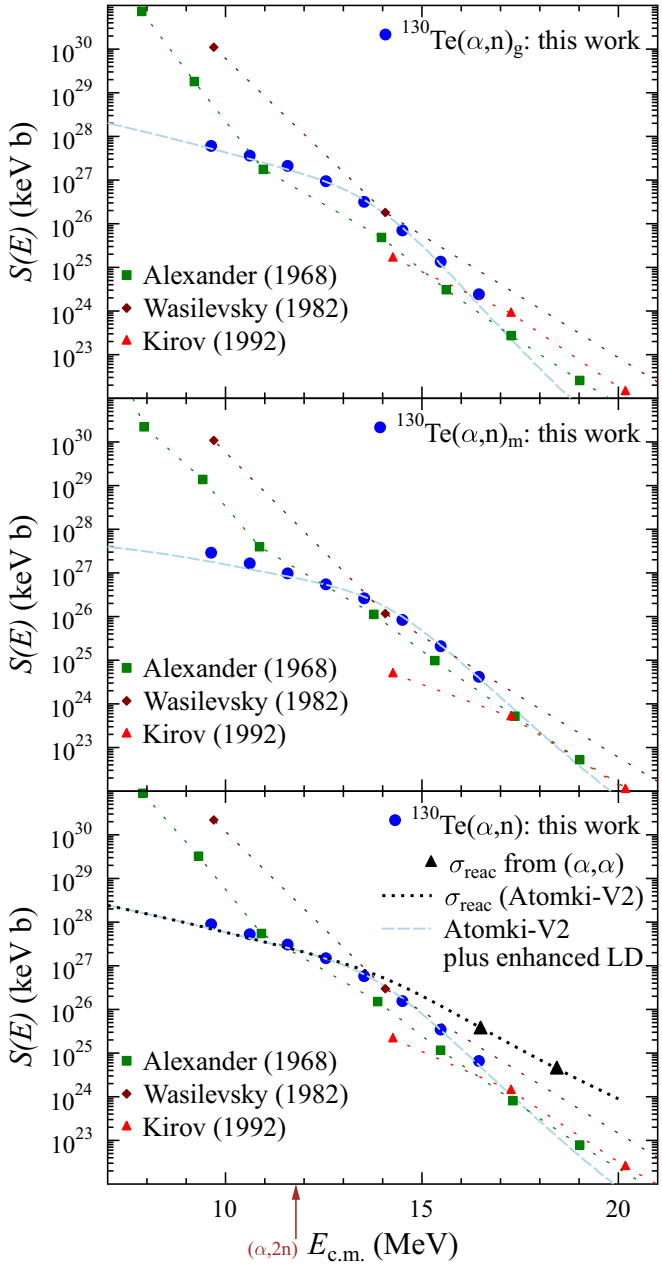

FIG. 14. Same as Figs. 12 and 13, but including experimental data from literature [50–52]. The data from each data set are connected by thin lines to guide the eye. A much larger scale is required to cover the wide scatter of the literature data. For further discussion see text.

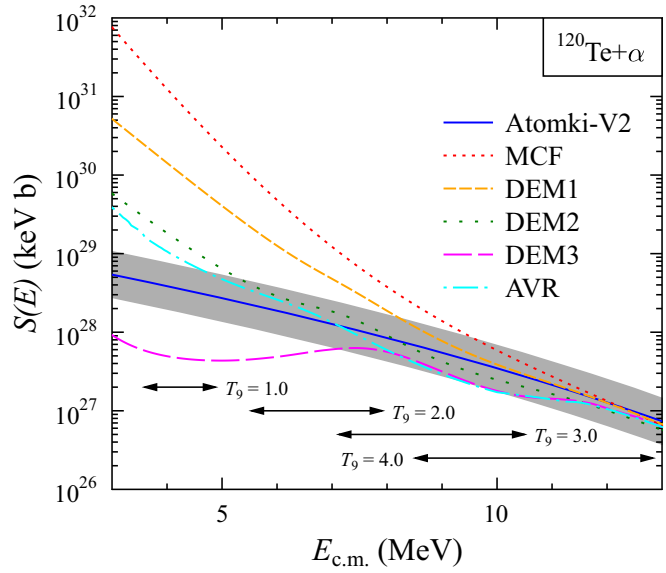

FIG. 15. Total cross section σ_{reac} of ^{120}Te + α at low energies (shown as astrophysical S factors). The claimed uncertainty of the Atomki-V2 AOMP is indicated by the grey-shaded area. The horizontal arrows indicate the classical Gamow windows for $T_9 = 1$, 2, 3, and 4. For further discussion see text.

found in the pioneering experiment on ^{144}Sm$(\alpha,\gamma)^{148}$Gd by Somorjai *et al.* [11] and confirmed by Scholz *et al.* [53], are not observed for the present (α, n) data. Such huge deviations are typically found only at deep sub-barrier energies which is below the (α, n) threshold for most heavy stable nuclei. This will be further investigated at the end of the discussion (see also Fig. 15 below).

Although the overall description of the new (α, n) data is good, there are significant differences between the various AOMPs under study. The (α, n) cross sections from the Atomki-V2 AOMP are closer to the new experimental data because these (α, n) cross sections are slightly higher than those from the other AOMPs under study. The reason for the relatively low (α, n) cross sections from the AVR AOMP is most likely the adjustment of the parameters–among others–to the relatively low cross sections measured by Palumbo *et al.* [39] for the ^{120}Te$(\alpha, n)^{123}$Xe reaction. There is no obvious explanation for the more or less pronounced underestimation of the (α, n) cross sections by the DEM1, DEM2, and DEM3 AOMPs. An undocumented modification of DEM1, DEM2, and DEM3 AOMPs in TALYS 1.96 sharpens the deviations to the new experimental data.

In general, the calculation of (α, n) cross sections is mainly sensitive to the chosen AOMP (as explained in Sec. IV A, IV B, IV D, and in Fig. 4). Other ingredients of the statistical model calculations play only a relatively minor role. Thus, further investigations beyond the AOMP were only necessary in two cases which are the ^{120}Te$(\alpha, n)^{123}$Xe and the ^{130}Te$(\alpha, n)^{133}$Xe reactions.

For ^{120}Te$(\alpha, n)^{123}$Xe, there is some tension between our new experimental data and the data by Palumbo *et al.* [39] close above the threshold. In this energy region, the contributions of the (α, n) and (α, γ) channels have the same order of magnitude. Whereas the new experimental data are nicely reproduced by the Atomki-V2 AOMP and TALYS default settings otherwise, the Palumbo data require an enhanced (α, γ) and reduced (α, n) channel which can be achieved e.g. by an enhancement of the GSF. Further experimental data close to the (α, n) threshold are required to resolve this issue (see Fig. 9).

For ^{130}Te$(\alpha, n)^{133}$Xe we find that the combination of the Atomki-V2 AOMP with default parameters underestimates the new (α, n) data at higher energies. However, as the

Atomki-V2 AOMP reproduces the total cross section σ_{reac} (as determined by elastic scattering), the reason for the underestimation of the (α, n) cross sections must be related to other ingredients of the statistical model. It is found that the (α, n) data can be nicely described by an enhancement of the LD in the residual ^{133}Xe nucleus which favors the (α, n) channel and reduces the otherwise far dominating $(\alpha, 2n)$ channel at energies above 14 MeV (see Fig. 13).

In general, it has to be pointed out that additional experimental data for other reaction channels like (α, γ) or (α, p) or $(\alpha, 2n)$ or isomer branchings are required to constrain the other ingredients of the statistical model beyond the AOMP. As the availability of such additional data is very limited, the other ingredients of the statistical model like the GSF and the LD cannot be well constrained.

Finally, we study the low-energy behavior of the AOMPs for the example of the ^{120}Te$(\alpha, \gamma)^{124}$Xe reaction. As already shown in Fig. 4, at low energies below the (α, n) threshold around 10 MeV, the (α, γ) cross section is practically identical to the total cross section σ_{reac}. Thus, for simplicity we investigate only σ_{reac} in the following. The result is shown in Fig. 15 down to deep sub-barrier energies.

Whereas at higher energies the Atomki-V2 AOMP provides the highest σ_{reac}, the other AOMPs show much higher σ_{reac} towards very low energies. Below about 10 MeV most of the other AOMPs (except the DEM3 AOMP) show a more or less pronounced steep increase of the S factor towards lower energies. This steep increase is typically related to the tail of the imaginary part of the AOMP at large radii beyond the colliding nuclei which is not well constrained (for a detailed discussion see [54] and the Supplemental Material of [40]). At 10 MeV the predicted total cross sections vary by about a factor of 2.4 among the AVR, DEM1, DEM2, DEM3, and Atomki-V2 AOMPs. (We exclude the MCF AOMP from the discussion because the dramatic overestimation of low-energy S factors is well known and confirmed here.) The range of predictions from the AVR, DEM1, DEM2, DEM3, and Atomki-V2 AOMPs increases to factors of 9.5 at 7.5 MeV and 84.9 at 5.0 MeV. Thus, huge discrepancies between the predictions from various AOMPs reappear also in the present study of α-induced reactions on tellurium isotopes, but only at energies far below the Coulomb barrier.

Figure 15 also shows the claimed uncertainty of a factor of two for the Atomki-V2 AOMP. It is interesting to note that the AVR and DEM2 AOMPs remain within this uncertainty range at all energies above about 5 MeV. For the DEM1 and DEM3 AOMPs this holds above 8 MeV and 7 MeV, respectively.

Because of the overall good description of the present (α, n) cross sections from the Atomki-V2 AOMP, we do not provide new astrophysical reaction rates in this paper. Instead, we recommend to use the reaction rates from the Atomki-V2 AOMP for all tellurium isotopes which are published in [43] and available for numerical download.

V. SUMMARY AND CONCLUSIONS

In the present work, the (α, n) cross section of four Te isotopes (^{120,122,124,130}Te) was measured between 10 and 17 MeV α energies using the activation technique. For these reactions experimental data were not at all available in the literature, or not in the presently studied energy range and with sufficiently high precision. In the case of the ^{130}Te $(\alpha, n)^{133}$Xe reaction the cross section leading to the ground and isomeric states of ^{133}Xe were measured separately.

Since the cross sections were measured close above the (α, n) thresholds, the results allow the study of the α-nucleus optical potential, which is an important quantity in various nuclear astrophysics models. The new experimental data were compared with statistical model predictions using various AOMP models. It is found that the recently developed Atomki-V2 potential gives the best description of the experimental data. This result provides a further proof of the generally good predictive power of this potential in this mass and energy range. The application of the recently compiled reaction rates based on this potential [43] is thus recommended in nucleosynthesis calculations.

ACKNOWLEDGMENTS

This work was supported by NKFIH Grants No. NN128072, No. K134197, and No. K138031 and by the ÚNKP-23-3-I-DE-165 New National Excellence Programs of the Ministry for Culture and Innovation of Hungary. The financial support of the Hungarian Academy of Sciences (Infrastructure Grants) and the Economic Development and Innovation Operational Programme (GINOP-2.3.3–15-2016-00005) grant, cofunded by the EU, is also acknowledged.

[1] C. Iliadis, *Nuclear Physics of Stars* (Wiley, New York, 2015).
[2] W. Hauser and H. Feshbach, Phys. Rev. **87**, 366 (1952).
[3] T. Rauscher, Int. J. Mod. Phys. E **20**, 1071 (2011).
[4] M. Arnould and S. Goriely, Phys. Rep. **384**, 1 (2003).
[5] T. Rauscher, N. Dauphas, I. Dillmann, C. Fröhlich, Z. Fülöp, and G. Gyürky, Rep. Prog. Phys. **76**, 066201 (2013).
[6] F. Käppeler, R. Gallino, S. Bisterzo, and W. Aoki, Rev. Mod. Phys. **83**, 157 (2011).
[7] M. Lugaro, M. Pignatari, R. Reifarth, and M. Wiescher, Annu. Rev. Nucl. Part. Sci. **73**, 315 (2023).
[8] J. J. Cowan, C. Sneden, J. E. Lawler, A. Aprahamian, M. Wiescher, K. Langanke, G. Martínez-Pinedo, and F.-K. Thielemann, Rev. Mod. Phys. **93**, 015002 (2021).
[9] G. G. Kiss, P. Mohr, G. Gyürky, T. Szücs, L. Csedreki, Z. Halász, Z. Fülöp, and E. Somorjai, Phys. Rev. C **106**, 015802 (2022).
[10] L. McFadden and G. R. Satchler, Nucl. Phys. **84**, 177 (1966).
[11] E. Somorjai, Z. Fülöp, A. Z. Kiss, C. E. Rolfs, H. P. Trautvetter, U. Greife, M. Junker, S. Goriely, M. Arnould, M. Rayet *et al.*, Astron. Astrophys. **333**, 1112 (1998).
[12] D. Basak and C. Basu, Eur. Phys. J. A **58**, 150 (2022).
[13] P. Mohr, Z. Fülöp, and H. Utsunomiya, Eur. Phys. J. A **32**, 357 (2007).
[14] T. Rauscher, AIP Adv. **4**, 041012 (2014).

[15] G. Gyürky, P. Mohr, A. Angyal, Z. Halász, G. G. Kiss, Z. Mátyus, T. N. Szegedi, T. Szücs, and Z. Fülöp, Phys. Rev. C **107**, 025803 (2023).
[16] P. Mohr, Phys. Rev. C **94**, 035801 (2016).
[17] A. Arcones and F. Montes, Astrophys. J. **731**, 5 (2011).
[18] T. N. Szegedi, G. G. Kiss, P. Mohr, A. Psaltis, M. Jacobi, G. G. Barnaföldi, T. Szücs, G. Gyürky, and A. Arcones, Phys. Rev. C **104**, 035804 (2021).
[19] A. Psaltis, A. Arcones, F. Montes, P. Mohr, C. J. Hansen, M. Jacobi, and H. Schatz, Astrophys. J. **935**, 27 (2022).
[20] G. G. Kiss, T. N. Szegedi, P. Mohr, M. Jacobi, G. Gyürky, R. Huszánk, and A. Arcones, Astrophys. J. **908**, 202 (2021).
[21] J. Meija, T. B. Coplen, M. Berglund, W. A. Brand, P. D. Bièvre, M. Gröning, N. E. Holden, J. Irrgeher, R. D. Loss, T. Walczyk *et al.*, Pure Appl. Chem. **88**, 293 (2016).
[22] R. Murugan, T. Aono, and S. K. Sahoo, Molecules **25**, 1956 (2020).
[23] Gy. Gyürky, Zs. Fülöp, F. Käppeler, G. G. Kiss, and A. Wallner, Eur. Phys. J. A **55**, 41 (2019).
[24] J. Chen, Nucl. Data Sheets **174**, 1 (2021).
[25] J. Katakura, Nucl. Data Sheets **112**, 495 (2011).
[26] A. Hashizume, Nucl. Data Sheets **112**, 1647 (2011).
[27] Y. Khazov, A. Rodionov, and F. Kondev, Nucl. Data Sheets **112**, 855 (2011).
[28] T. Szegedi, G. Kiss, I. Öksüz, T. Szücs, G. Gyürky, Z. Elekes, E. Somorjai, and Z. Fülöp, Nucl. Phys. A **986**, 213 (2019).
[29] I. Rajta, I. Vajda, Gy. Gyürky, L. Csedreki, A. Kiss, S. Biri, H. van Oosterhout, N. Podaru, and D. Mous, Nucl. Instrum. Methods Phys. Res., Sect. A **880**, 125 (2018).
[30] M. Mayer, SIMNRA version 6.06, https://mam.home.ipp.mpg.de/.
[31] L. Bartha and I. Uzonyi, Nucl. Instrum. Methods Phys. Res., Sect. B **161-163**, 339 (2000).
[32] J. Campbell, N. Boyd, N. Grassi, P. Bonnick, and J. Maxwell, Nucl. Instrum. Methods Phys. Res., Sect. B **268**, 3356 (2010).
[33] S. Biri, I. K. Vajda, P. Hajdu, R. Rácz, A. Csík, Z. Kormány, Z. Perduk, F. Kocsis, and I. Rajta, Eur. Phys. J. Plus **136**, 247 (2021).
[34] Z. Korkulu, N. Özkan, G. G. Kiss, T. Szücs, G. Gyürky, Z. Fülöp, R. T. Güray, Z. Halász, T. Rauscher, E. Somorjai *et al.*, Phys. Rev. C **97**, 045803 (2018).
[35] J. Ziegler, SRIM-2013 software code, http://srim.org/.
[36] P. Demetriou, C. Grama, and S. Goriely, Nucl. Phys. A **707**, 253 (2002).
[37] M. Avrigeanu, W. von Oertzen, A. Plompen, and V. Avrigeanu, Nucl. Phys. A **723**, 104 (2003).
[38] V. Avrigeanu, M. Avrigeanu, and C. Mănăilescu, Phys. Rev. C **90**, 044612 (2014).
[39] A. Palumbo, W. P. Tan, J. Görres, M. Wiescher, N. Özkan, R. T. Güray, and C. Yalçın, Phys. Rev. C **85**, 028801 (2012).
[40] P. Mohr, Z. Fülöp, G. Gyürky, G. G. Kiss, and T. Szücs, Phys. Rev. Lett. **124**, 252701 (2020).
[41] P. Mohr, G. Kiss, Z. Fülöp, D. Galaviz, G. Gyürky, and E. Somorjai, At. Data Nucl. Data Tables **99**, 651 (2013).
[42] W.-J. Ong, M. L. Avila, P. Mohr, K. E. Rehm, D. Santiago-Gonzalez, J. Chen, C. R. Hoffman, Z. Meisel, F. Montes, and J. Pereira, Phys. Rev. C **105**, 055803 (2022).
[43] P. Mohr, Z. Fülöp, G. Gyürky, G. G. Kiss, T. Szücs, A. Arcones, M. Jacobi, and A. Psaltis, At. Data Nucl. Data Tables **142**, 101453 (2021).
[44] T. Rauscher and F.-K. Thielemann, At. Data Nucl. Data Tables **75**, 1 (2000).
[45] A. J. Koning, S. Hilaire, and S. Goriely, computer code TALYS, 2017, http://www.talys.eu/.
[46] A. Koning, S. Hilaire, and S. Goriely, Eur. Phys. J. A **59**, 131 (2023).
[47] A. Palumbo, W. P. Tan, J. Görres, A. Best, M. Couder, R. Crowter, R. J. deBoer, S. Falahat, P. J. LeBlanc, H. Y. Lee *et al.*, Phys. Rev. C **85**, 035808 (2012).
[48] S. Salém Vasconcelos, M. Rao, N. Ueta, and C. Appoloni, Nucl. Phys. A **313**, 333 (1979).
[49] S. Goriely (private communication).
[50] A. Kirov, N. Nenoff, and D. Kolev, Z. Phys. A: Hadrons Nucl. **341**, 443 (1992).
[51] C. Wasilevsky, R. Montenegro, M. de la Vega Vedoya, and S. J. Nassiff, Radiochem. Radioanal. Lett. **50**, 307 (1982).
[52] P. Alexander and J. P. Lau, Nucl. Phys. A **121**, 612 (1968).
[53] P. Scholz, H. Wilsenach, H. W. Becker, A. Blazhev, F. Heim, V. Foteinou, U. Giesen, C. Münker, D. Rogalla, P. Sprung *et al.*, Phys. Rev. C **102**, 045811 (2020).
[54] T. Szücs, P. Mohr, G. Gyürky, Z. Halász, R. Huszánk, G. G. Kiss, T. N. Szegedi, Z. Török, and Z. Fülöp, J. Phys.: Conf. Ser. **1668**, 012042 (2020).